

See discussions, stats, and author profiles for this publication at: <https://www.researchgate.net/publication/221807312>

Antifreeze Protein from Freeze-Tolerant Grass Has a Beta-Roll Fold with an Irregularly Structured Ice-Binding Site

ARTICLE *in* JOURNAL OF MOLECULAR BIOLOGY · MARCH 2012

Impact Factor: 4.33 · DOI: 10.1016/j.jmb.2012.01.032 · Source: PubMed

CITATIONS

37

READS

66

8 AUTHORS, INCLUDING:



[Maya Bar Dolev](#)

Hebrew University of Jerusalem

24 PUBLICATIONS 180 CITATIONS

SEE PROFILE



[Ido Braslavsky](#)

Hebrew University of Jerusalem

70 PUBLICATIONS 1,178 CITATIONS

SEE PROFILE



[Robert L Campbell](#)

Queen's University

62 PUBLICATIONS 1,913 CITATIONS

SEE PROFILE



[Virginia Walker](#)

Queen's University

168 PUBLICATIONS 4,039 CITATIONS

SEE PROFILE



Antifreeze Protein from Freeze-Tolerant Grass Has a Beta-Roll Fold with an Irregularly Structured Ice-Binding Site

Adam J. Middleton¹, Christopher B. Marshall², Frédérick Faucher¹, Maya Bar-Dolev³, Ido Braslavsky³, Robert L. Campbell¹, Virginia K. Walker^{1,4} and Peter L. Davies^{1*}

¹Department of Biomedical and Molecular Sciences, Queen's University, Kingston, Ontario, Canada K7L 3N6

²University Health Network, Toronto, Ontario, Canada M5G 1L7

³The Robert H. Smith Faculty of Agriculture, Food, and Environment Sciences, The Hebrew University of Jerusalem, Rehovot 76100, Israel

⁴Department of Biology, Queen's University, Kingston, Ontario, Canada K7L 3N6

Received 9 December 2011;

accepted 18 January 2012

Available online

28 January 2012

Edited by R. Huber

Keywords:

ice recrystallization
inhibition;
X-ray crystallography;
beta-helix;
water;
thermolabile

The grass *Lolium perenne* produces an ice-binding protein (*LpIBP*) that helps this perennial tolerate freezing by inhibiting the recrystallization of ice. Ice-binding proteins (IBPs) are also produced by freeze-avoiding organisms to halt the growth of ice and are better known as antifreeze proteins (AFPs). To examine the structural basis for the different roles of these two IBP types, we have solved the first crystal structure of a plant IBP. The 118-residue *LpIBP* folds as a novel left-handed beta-roll with eight 14- or 15-residue coils and is stabilized by a small hydrophobic core and two internal Asn ladders. The ice-binding site (IBS) is formed by a flat beta-sheet on one surface of the beta-roll. We show that *LpIBP* binds to both the basal and primary-prism planes of ice, which is the hallmark of hyperactive AFPs. However, the antifreeze activity of *LpIBP* is less than 10% of that measured for those hyperactive AFPs with convergently evolved beta-solenoid structures. Whereas these hyperactive AFPs have two rows of aligned Thr residues on their IBS, the equivalent arrays in *LpIBP* are populated by a mixture of Thr, Ser and Val with several side-chain conformations. Substitution of Ser or Val for Thr on the IBS of a hyperactive AFP reduced its antifreeze activity. *LpIBP* may have evolved an IBS that has low antifreeze activity to avoid damage from rapid ice growth that occurs when temperatures exceed the capacity of AFPs to block ice growth while retaining the ability to inhibit ice recrystallization.

© 2012 Elsevier Ltd. All rights reserved.

*Corresponding author. E-mail address:
peter.davies@queensu.ca.

Abbreviations used: *LpIBP*, *Lolium perenne* ice-binding protein; AFP, antifreeze protein; TH, thermal hysteresis; IRI, ice recrystallization inhibition; IBP, ice-binding protein; IBS, ice-binding site; CfAFP, *Choristoneura fumiferana* antifreeze protein; TmAFP, *Tenebrio molitor* antifreeze protein; FIPA, fluorescence-based ice plane affinity; GFP, green fluorescent protein; MpAFP, *Marinomonas primoryensis* antifreeze protein.

Introduction

Antifreeze proteins (AFPs) are found in diverse organisms ranging from vertebrates to bacteria that are exposed to sub-freezing environments at some point in their life histories.^{1–4} Two frequently measured activities of AFPs are depression of the freezing point relative to the melting point, referred to as thermal hysteresis (TH),⁵ and ice recrystallization inhibition (IRI).⁶ TH activity halts ice crystal

growth, allowing freeze-intolerant organisms (such as fish and some insects) to supercool and avoid freezing. IRI activity is more relevant in freeze-tolerant organisms, which are unable to avoid freezing and therefore must minimize the damage caused by recrystallization of ice in frozen tissue.⁷ For example, some overwintering plants such as carrots and grasses produce proteins that show weak TH activity but have IRI activity matching or exceeding that of fish and insect AFPs.^{8–10} The structural basis for the differences in these activities is one of the issues addressed in this work. Because some proteins with TH activity function as IRI proteins rather than antifreezes, we introduce the more inclusive term “ice-binding protein” (IBP) to refer to proteins that serve in either capacity.¹¹

IBPs irreversibly adsorb to the surface of ice crystals and inhibit their growth by the Gibbs–Thomson effect,¹² in which the addition of water molecules to the ice lattice is limited to the space between bound IBPs, resulting in surface curvature that makes the further addition of water thermodynamically unfavorable.¹³ Recent work suggests that IBPs adsorb to ice through an ordered ice-like array of waters assembled by the protein's ice-binding site (IBS), which merges with and freezes to the ice surface.^{14–16} The spacing of these so-called “clathrate” waters, anchored to the IBP by hydrogen bonds, matches one or more planes of ice. In this anchored-clathrate mechanism, the IBP essentially preforms part of its ligand before irreversibly adhering to it.

AFP were recognized in certain insects over 30 years ago.^{17–19} More recently, characterization of purified insect AFPs revealed that their specific TH activities exceed those of fish AFPs by an order of magnitude;^{20,21} thus, they were termed “hyperactive.” The heightened TH of hyperactive *versus* moderately active AFPs has been attributed to their unique affinity for the basal plane of ice.²² Moderately active AFPs bind only to prism and/or pyramidal planes, leaving the basal planes unprotected and vulnerable to growth.^{23–27} Although the addition of water to the basal planes of ice is less favorable than to a prism surface, this readily occurs under supercooled conditions when the TH gap of moderately active AFPs is exceeded, resulting in rapid crystal growth along the *c*-axis. Adsorption of AFPs to the basal plane provides substantially better coverage of the ice crystal and therefore provides greater TH activity.

The perennial ryegrass *Lolium perenne* is a freeze-tolerant forage grass planted worldwide²⁸ that thrives in cold environments.^{29,30} An IBP isolated from *L. perenne* (*LpIBP*) was reported to have high IRI but low TH activity.⁸ *LpIBP* TH activity is an order of magnitude lower than that of hyperactive AFPs and slightly less than that of moderately active fish type I, II and III AFPs.³¹ However, it has superior IRI activity.^{8,10} Subsequently, several iso-

forms and homologues of this IBP have been found in various grasses in the sub-family *Pooideae*.³² The protein originally isolated constitutes the highly repetitive C-terminal “IRI” domain of a longer protein. On the basis of the DNA sequence, the complete protein includes an N-terminal secretion signal sequence and a leucine-rich repeat domain, but the ice-binding activity is limited to the IRI domain, which may represent the fully processed form of the protein. *LpIBP* is secreted from plant cells and functions in the apoplast, where it acts to minimize frost damage to the plant tissue, largely through its IRI activity.²⁸

The sequence of the highly repetitive C-terminal domain of *LpIBP* suggested that its structure might resemble other beta-solenoid proteins, in particular the hyperactive AFPs discovered in the insects *Tenebrio molitor* (*TmAfp*) and *Choristoneura fumiferana* (*CfAFP*).^{33,34} This was supported by a computer model of this protein as a right-handed beta-roll with two flat beta-sheets on opposite sides of the solenoid termed “a” and “b” faces.³⁵ These flat surfaces resembled the IBSs of the insect AFPs, and it was originally proposed that both sheets might simultaneously bind ice on opposite sides of *LpIBP*. However, it was subsequently determined experimentally that only one of the two flat surfaces is responsible for TH activity.³¹ The introduction of single steric point mutations on the a face of *LpIBP* reduced the TH and IRI activities of the protein by up to 90%, whereas mutation of the b face had only a small effect.

Here, we report the X-ray crystal structure of *LpIBP*, which is the first such description of a plant IBP. Its structure resembles that of some of the hyperactive AFPs but with a less regular IBS, which we argue is the basis for its low TH activity. Like the hyperactive AFPs, *LpIBP* binds the basal plane of ice. Together, these analyses suggest that *LpIBP* has developed the ability to control ice growth at high sub-zero temperatures, which is compatible with a role in promoting freeze tolerance.

Results

Crystallization and structure determination of *LpIBP*

LpIBP crystallized in the monoclinic C2 space group with two molecules per asymmetric unit. Crystals were grown at low pH (4.2) and high concentrations of ethanol (40–50%) at 4 °C over approximately 4 weeks. Data were collected at beamline X6A at National Synchrotron Light Source in Brookhaven National Laboratories. Two data sets obtained from two crystals were combined to obtain phases using single isomorphous replacement with anomalous scattering. After solvent flattening, the

electron density map was well defined, and >95% of the model was built automatically by ARP/wARP.³⁶ The structure was refined at a resolution of 1.4 Å ($R_{\text{work}}=16.5\%$, $R_{\text{free}}=18.7\%$) and has a solvent content of 70% (Table 1). Only the first three residues (DEQ) of *LpIBP* and the C-terminal His-tag were not observed in the electron density map. In addition to the protein, 235 waters, 2 ethylene glycol molecules and 11 ethanol molecules were found. Asn69 in chain B was the only residue located in an unfavorable region of the Ramachandran plot, and this was due to steric hindrance imposed by crystal packing.

Table 1. Summary of data collection and refinement statistics

	Native	Iodide
<i>Data collection</i>		
Wavelength (Å)	1.13	1.55
Resolution (Å)	20–1.4 (1.5–1.4) ^a	20–2.1 (2.2–2.1)
Space group	C2	C2
Unit cell parameters		
<i>a</i> , <i>b</i> , <i>c</i> (Å)	94.28, 62.49, 44.00	94.7, 62.53, 44.05
β (°)	113.96	114.34
Total reflections	256,957 (42,228)	51,177 (3943)
Unique reflections	45,098 (8305)	23,468 (1969)
Completeness (%)	97.9 (96.9)	87.1 (56.9)
<i>I</i> / σ (<i>I</i>)	16.8 (5.5)	7.10 (2.8)
R_{merge} (%) ^b	5.7 (29.3)	7.3 (2.5)
Redundancy	5.7 (5.7)	2.2 (2)
Iodide sites		16
R_{cullis} ^c		
Acentric/centric/ anomalous ^c		0.75/0.82/0.9
Phasing power		
Acentric/centric/ anomalous		1.32/0.96/0.77
Overall mean figure of merit ^d		0.3/0.85
<i>Refinement</i>		
R_{work} (%) ^e	16.5	
R_{free} (%) ^e	18.7	
RMSD from ideal bond length (Å)/angles (°)	0.011/1.4	
Non-hydrogen atoms	2109	
All atoms	3850	
Protein	3496	
Water	235	
Other solvent atoms	117	
Average <i>B</i> -factors (Å ²)	17.3	
Ramachandran plot (%)		
Most favored regions	92.5	
Allowed regions	6.8	
Disallowed regions	0.7	

^a High-resolution shell is shown in parentheses.

^b $R_{\text{merge}} = P |I - \langle I \rangle| / PI$, where $\langle I \rangle$ is the average intensity from multiple observations of symmetry-related reflections.

^c $R_{\text{cullis}} = [(\langle \text{LOC} \rangle^2)_{1/2} (\langle |F|_2 \rangle)_{1/2}]$, where LOC is the lack-of-closure error.

^d Before and after density modification.

^e R_{work} and $R_{\text{free}} = P_h | |F_o| - |F_c| | / P_h |F_o|$, where F_o and F_c are the observed and calculated structure factor amplitudes, respectively. R_{free} was calculated with 5% of the reflections not used in refinement.

LpIBP is a left-handed beta-roll

The 118-residue protein folds as a left-handed beta-helix with a length of 33 Å, a width of 20 Å and a height of 10 Å (Fig. 1a). Each of the eight beta-helical coils is composed of two seven-residue tandem repeats with a consensus sequence XXNXVXG (Fig. 1b), where X is a solvent-exposed residue, typically with a polar side chain. The a side of the beta-roll is the beta-sheet made from the seven-residue repeats on the left-hand side of Fig. 1b, and the b side is the beta-sheet made from the seven-residue repeats on the right-hand side. The first three coils have one additional outward-pointing residue (Fig. 1c, red circle) inserted into each second repeat (b side) on the C-terminal side of the conserved Val (Fig. 1b, yellow highlight). This insertion causes a bulge in the cross-section of the coil (lower right quadrant in Fig. 1c), which is not present in the other five coils (Fig. 1d). The bulge in the b side is accompanied by the substitution of two larger hydrophobic residues (Ile7 and Leu22) for Val on the opposing a side in the N-terminal two coils. Together, these substitutions and insertions assemble a slightly larger hydrophobic core at the N-terminal end. Two residues (Asp–Glu) precede the first tandem repeat, and the last three residues of the C-terminal, eighth coil (Thr–Asp–Ala) deviate from the consensus sequence (Fig. 1b).

The beta-roll is stabilized by internal Asn/His ladders

Characteristic of a beta-solenoid, the structure is stabilized by backbone amide to carbonyl hydrogen bonds of which there are 83 predicted here between the parallel coils down the length of the protein (Fig. 2a). Within the core of the structure, adjacent coils are held together by two internal Asn ladders that run the length of the beta-roll. The Asn side-chain amide and carbonyl groups hydrogen bond to the main-chain atoms of neighboring coils and to adjacent Asn side chains (Fig. 2b) to help form the beta-arcades³⁷ that link the a and b sides of the beta-roll. His substitutes for Asn at four locations in the helix and their side-chain amide groups hydrogen bond only to main-chain atoms on adjacent coils (Fig. 2c). The conserved Gly residues at the end of each heptad repeat allow the protein to make acute beta-arches that tightly pack the highly conserved Val residues in the center of the core.

Comparative analysis of *LpIBP* structure

A search of the Protein Data Bank using one chain of *LpIBP* was performed using the Dali server (DaliLite v.3).³⁸ The top alignment was to an adhesin structure from the bacterium *Moraxella*

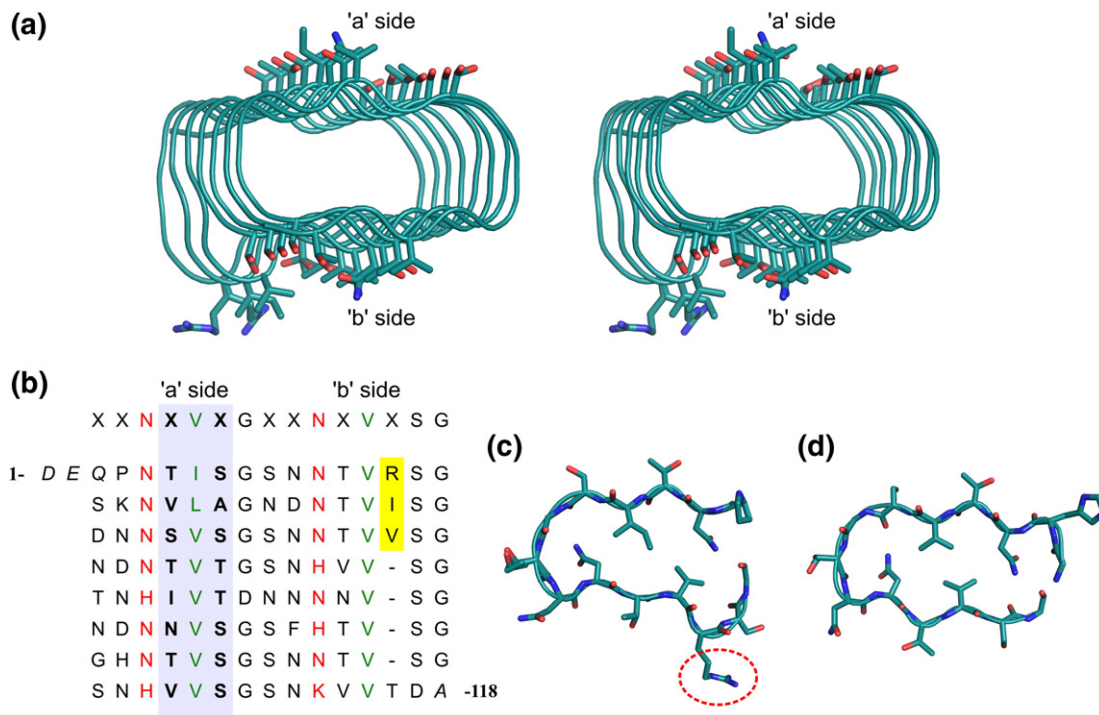


Fig. 1. Structure of *LpIBP*. (a) Stereo image of chain B of *LpIBP*. The main-chain atoms are shown in cartoon representation. Side chains on the a and b sides are shown as sticks. The C terminus is at the front, and the N terminus is at the back. Carbon atoms are cyan, nitrogen atoms are blue and oxygen atoms are red. (b) Sequence of *LpIBP* divided so that the two tandem repeats constituting a coil of the helix are on the same line. On top is the consensus sequence. Inward-pointing Asn or His are in red, the hydrophobic core is in green and the IBS is shown with a gray background. Highlighted in yellow are the one-amino-acid insertions in the first three coils. (c) Cross-section view of one of the first three coils (coil 1) showing that the hydrophobic packing is twisted to compensate for the extra residue (circled in dotted red) in the first three coils. (d) Cross-section view of one of the last five coils (coil 7). Coloring for (c) and (d) is the same as in (a).

*catarrhalis*³⁹ with a Z-score of 17.8 and an RMSD of 1.3 Å. The subsequent matches were primarily other prokaryotic adhesin proteins, though a bacteriophage tail spike protein⁴⁰ also scored highly (Z-score of 16.2). All of the high-scoring results were left-handed beta-helical structures composed of 14- to 16-residue tandem repeats. None of the top search results were eukaryotic proteins. The highest sequence identity was 23%, which is on the borderline for homology and probably reflects the abundance of certain amino acids (Asn, Ser, Thr and Val) in beta-solenoids³⁷ rather than a recognizable relationship by descent.

The IBS of *LpIBP* lacks the regularity of insect AFPs

The *ab initio* model of *LpIBP* was built as a beta-roll of opposite handedness (right handed) to this structure.³⁵ It correctly forecast the Val core and two Asn ladders. The model did not, however, anticipate the N-terminal bulge on the b side associated with the one-amino-acid insertions in

the first three coils. Instead, it predicted two extensive, flat surfaces (a and b sides) on the protein, one or both of which were proposed to bind ice. Here, the X-ray crystal structure shows that the flatness of the b side is disrupted by this bulge. However, the a side is extraordinarily flat with each coil packing in almost perfect alignment with its neighbors, which is consistent with a site-directed mutagenesis study that mapped the IBS to the a side.³¹ Unlike most beta-solenoids,³⁷ *LpIBP* does not display a twist. The lack of twist from one coil to the next ensures that the IBS is flat for engaging the surface on an ice plane.

Flat, untwisted IBSs supported by beta-helical scaffolds have been seen before in two nonhomologous insect AFPs,^{33,34} both of which have two parallel arrays of Thr, assembled from beta-strands bearing TXT motifs, where X is any inward-pointing residue (Fig. 3a). The IBS Thr residues of these hyperactive insect AFPs are all fixed in the same rotameric conformation such that the distance between equivalent side-chain atoms closely matches the spacing of O atoms in two dimensions

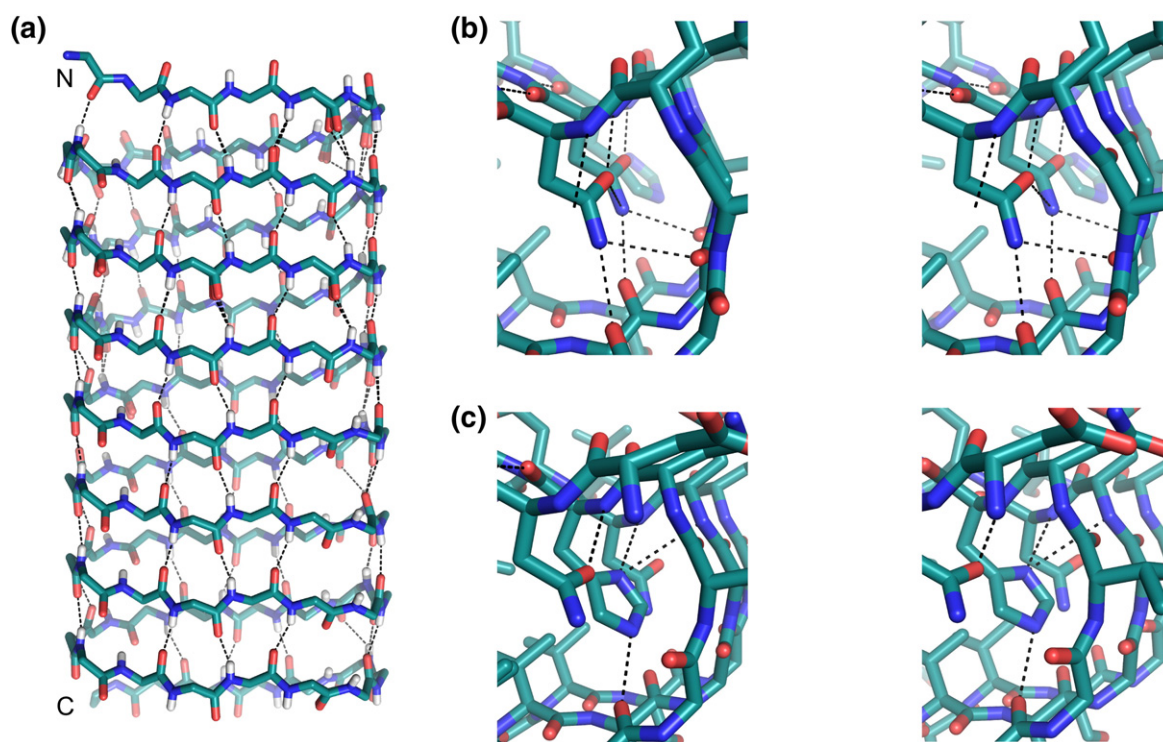


Fig. 2. Stabilization of the structure of *LpIBP*. (a) The structure of *LpIBP* highlighting the extensive main-chain hydrogen bonds. N and C termini are indicated. (b) Stereo view of the hydrogen-bonding network of the Asn ladder and (c) the His ladder. Coloring is identical with Fig. 1a.

on both the primary-prism and basal planes of ice.^{33,34,41} However, the IBS residues of *LpIBP* are less regular (Fig. 1a). Only 5 of the 16 positions are occupied by Thr (Fig. 1b), while the other 11 positions are occupied by Ser (6), Val (2), Ala (1), Ile (1) and Asn (1). Consequently, the side chains of these residues are not locked in particular orientations, and many were found in multiple conformations in the crystal structure (Fig. 3b). The conformational variability of the *LpIBP* IBS residues complicates measurement of the distances between neighboring side chains; thus, we measured the distances between the alpha carbon atoms to assess the regularity of the underlying beta-sheet. The ~ 6.8 -Å spacing between residues on the same beta-strand and 4.5 Å distance between adjacent residues on neighboring beta-strands (Fig. 3b) are similar to the spacing observed on the IBSs of other beta-helical AFPs^{15,33} (Fig. 3a) and approximate the spacing of water molecules on the basal and primary-prism planes of ice.

***LpIBP* contains rows of bound water molecules on its IBS**

The *LpIBP* crystal packing left the IBSs of both molecules in the asymmetric unit exposed in solvent channels (Fig. 4a). With the exception of an AFP

from the Antarctic bacterium *Marinomonas primoryensis* (*MpAFP*),¹⁵ every previous AFP structure solved by X-ray crystallography is derived from crystals in which proteins were packed IBS to IBS, either eliminating or restricting the number of surface waters. Due to fortuitous crystal packing, the *MpAFP* structure showed an extensive ice-like arrangement of waters around its IBS. Similarly, the IBS of *LpIBP* contains two rows of waters located in the troughs formed between the outward-pointing X residues of the XNXVX repeat (spaced ca 3.9–5.5 Å). However, these water molecules are less regular than the “anchored-clathrate” waters of *MpAFP*. Due to the high concentration of ethanol used under the crystallization condition, some waters are replaced with ethanol molecules. Most of these ethanols are oriented so that their hydroxyls occupy similar positions as adjacent water molecules. The *LpIBP*-bound waters are stabilized by hydrogen bonds to main-chain carbonyl groups as well as side-chain hydroxyls of threonine or serine residues. The distance between the two water rows on the IBS is approximately 7.0 Å, which is close to the spacing of oxygen atoms on the basal plane of ice (7.3 Å). Waters are also seen between the outward-pointing X residues of the XNX repeat on the non-IBS side spaced 4.5–5.0 Å apart (where N is part of an internal Asn ladder). A superimposition of the two

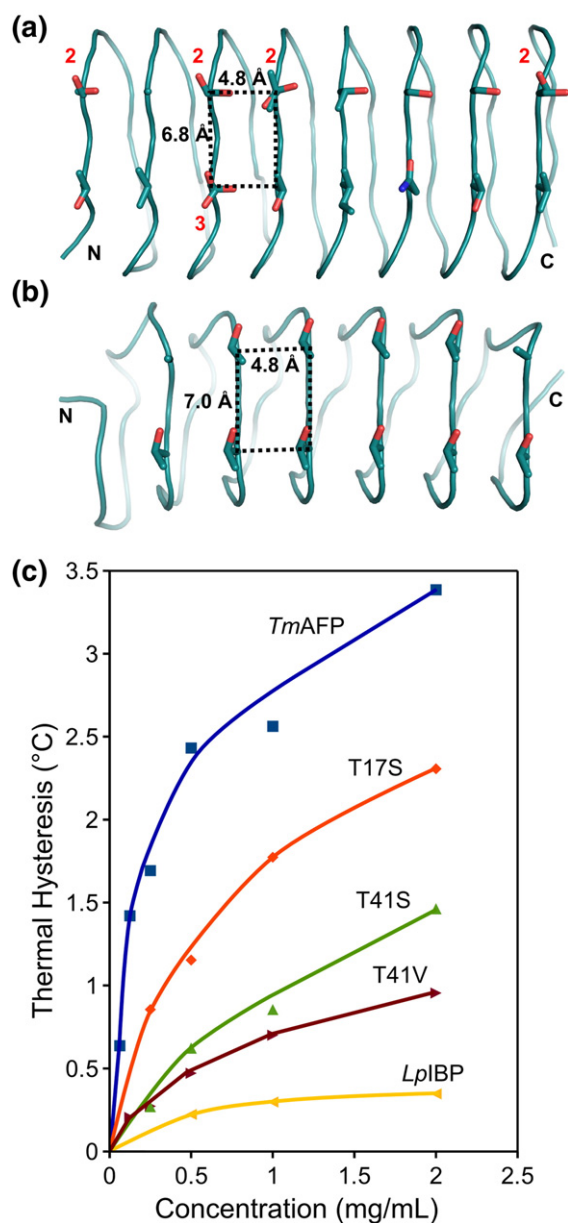


Fig. 3. *LpIBP* IBS. (a) View from above the IBS of *LpIBP* with the ice-binding residues shown as sticks. Numbers in red indicate the number of alternate conformations of side chains on the IBS. (b) *TmAFP* with the ice-binding side chains shown as sticks. Coloring is as in Fig. 1a. Black numbers in (a) and (b) show the spacing of the alpha carbons. N and C termini are indicated. (c) TH activity curve of *TmAFP* and mutations of *TmAFP*. Letters and number show threonine mutations made to *TmAFP*, and wild-type *LpIBP* activity is shown for comparison. The activity curves for the *TmAFP* mutations T17V, T39V and T39S were indistinguishable from those for T17S, T41S and T41V, respectively. The latter three curves were not included on the graph for clarity.

LpIBP molecules in the asymmetric unit shows that these waters occupy almost identical positions in both chains.

Effect of Thr replacements on the IBS of another beta-helical AFP

To examine the hypothesis that the low TH activity of *LpIBP* might be due to the presence of residues other than Thr on its IBS, we explored the impact of similar mutations on the TH activity of the beetle AFP *TmAFP*. Thr residues at position 17, 39 or 41 on the IBS of *TmAFP* were separately mutated to Ser and Val, and the TH activity of the pure protein was measured (Fig. 3c). All six mutations significantly lowered the TH activity of the AFP by 30–65% without disrupting the protein fold. Mutations of the centrally located Thr (positions 39 and 41) to either Ser or Val were the most deleterious. At a similar concentration, wild-type *LpIBP* has TH activity of 10% of wild-type *TmAFP* (Fig. 3c).³¹

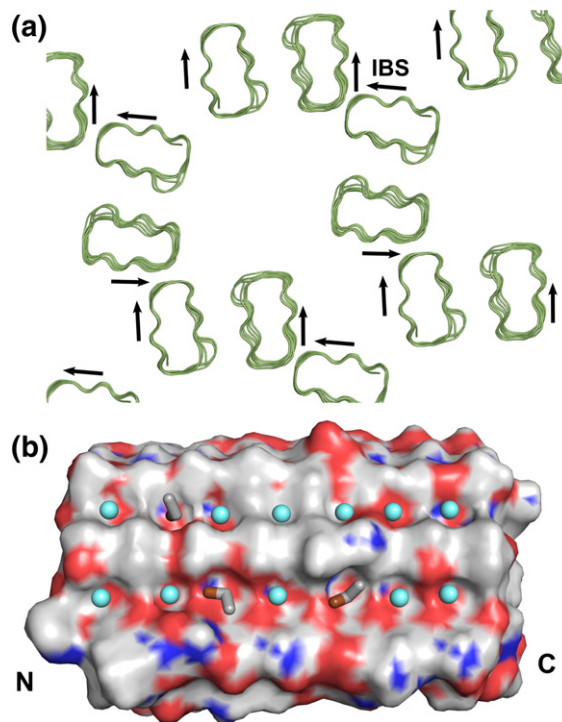


Fig. 4. Ordered surface waters on the crystal structure of *LpIBP*. (a) The packing of molecules in the crystal of *LpIBP*. Arrows represent the solvent-exposed IBS of *LpIBP*. The two molecules constituting the asymmetric unit are packed with the face opposite the IBS in contact. The beta-roll of *LpIBP* is depicted in cartoon representation. (b) Surface representation of *LpIBP*. Carbon is in white, nitrogen is in blue and oxygen is in red. N and C termini are shown. Light-blue spheres show the location of ordered water molecules on the IBS of the structure of *LpIBP*. Gray and brown sticks show locations of ethanol molecules found on the IBS. Carbon is in gray, and oxygen is in brown.

***Lp*IBP binds to the basal and primary-prism planes of ice**

To determine the planes of ice to which *Lp*IBP binds, we fluorescently labeled the protein with an N-terminal green fluorescent protein (GFP) tag. This construct was slowly incorporated into a growing single crystal ice hemisphere and directly visualized under UV illumination. An ice crystal oriented with the cold finger perpendicular to the basal plane exhibited a central, circular fluorescent patch on the basal plane surrounded by six evenly spaced patches on the primary-prism planes (Fig. 5a, *c*-axis perpendicular to the page). A hemisphere mounted with the basal plane parallel with the cold finger displayed three elongated fluorescent patches on the prism planes (Fig. 5b). For comparison, the fluorescence-based ice plane affinity (FIPA) analysis obtained with GFP-*Tm*AFP showed complete

coverage of the ice crystal hemisphere with no separate patches observed (Fig. 5c).

Binding to the basal plane of ice (in addition to other planes) is the hallmark of hyperactive AFPs.²² Within the TH gap, the supercooled ice crystal formed in the presence of *Lp*IBP had the general shape of a hexagonal bipyramid with the *c*-axis oriented between the two crystal tips (Fig. 5d). When the sample was cooled below the TH gap, the *Lp*IBP-bound ice crystal rapidly expanded along the *a*-axes while presenting flat basal planes that advanced only slowly (Fig. 5d). This morphology is consistent with the basal-plane affinity of *Lp*IBP.

Discussion

Here, we have presented the first structure of a plant “antifreeze protein,” which is in effect the first

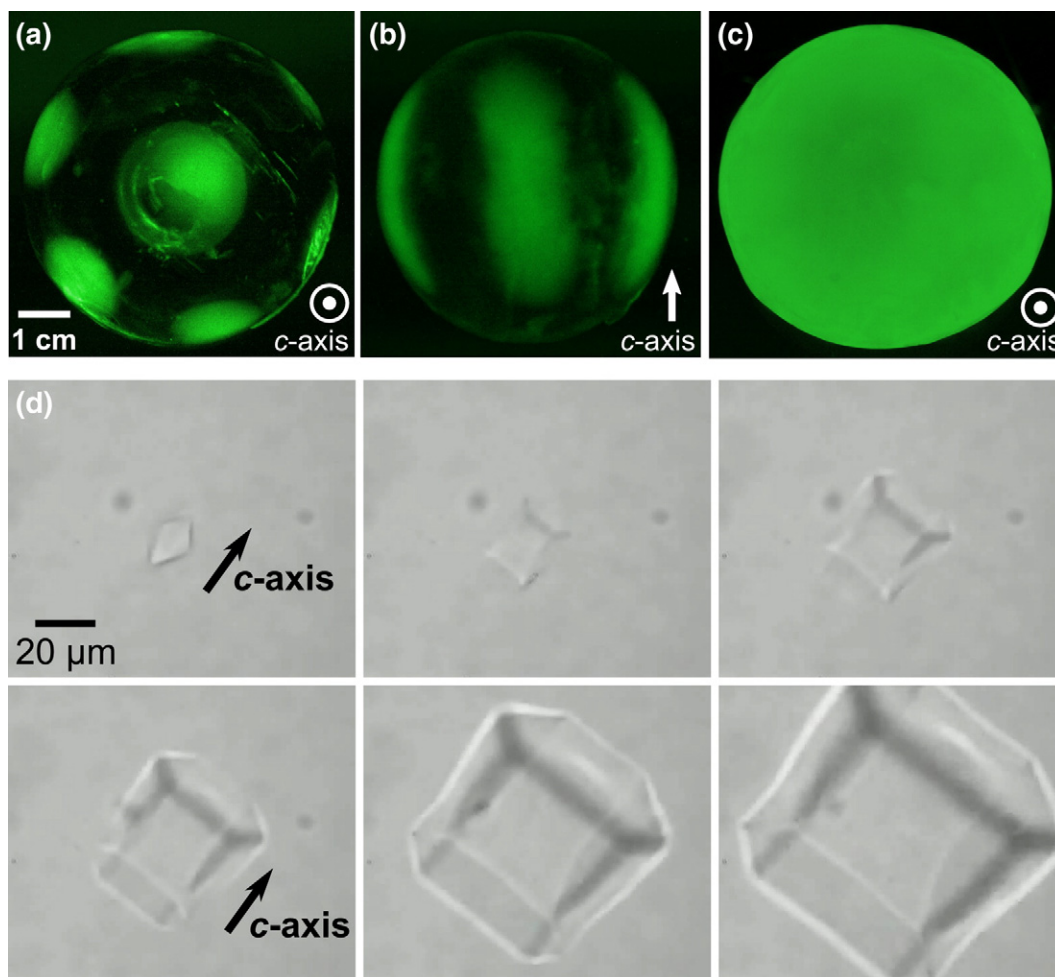


Fig. 5. Ice planes bound by *Lp*IBP. (a) An ice hemisphere was slowly grown in a solution of GFP-*Lp*IBP from a single crystal oriented with the *c*-axis perpendicular to the page and visualized under UV light. (b) An ice hemisphere was grown as in (a) with the *c*-axis vertical in the plane of the page as indicated. (c) Ice hemisphere grown in the presence of GFP-tagged *Tm*AFP. (d) Growth of a supercooled microscopic ice crystal in the presence of *Lp*IBP at 1 mg/mL. The melting point of the ice crystal was -0.57°C , and its freezing point was -0.86°C . The six frames encompass a period of 5 s.

structure of an IBP that functions primarily in freeze tolerance by inhibiting ice recrystallization. The fish and insect AFP structures solved to date^{25,33,34,42–46} all come from organisms that must avoid freezing. The repetitive, beta-helical *LpIBP* structure provides a flat regular ice-binding face that resembles several AFPs, most notably the hyperactive AFPs from insects. With its eight coils, *LpIBP* is similar in size and length to two insect beta-helical AFP structures, *TmAFP* and *CfAFP*, whereas it is notably shorter than the beta-helical AFP structure from the bacterium *M. primoryensis* (*MpAFP*), which is composed of 13 coils.^{15,33,34}

Unlike the insect AFPs, *TmAFP* and *CfAFP*, which are reinforced by disulfide bonds, and *MpAFP*, where internal calcium-ion coordination strengthens and rigidifies the fold, *LpIBP* is stabilized largely by an extensive hydrogen-bonding network within the external sheath and inner Asn/His ladder, as well as a small hydrophobic core. The low temperatures at which IBPs function strengthen hydrogen bonding but diminish the hydrophobic effect. A number of AFPs rely almost entirely on hydrogen bonding for their stability and like *LpIBP* have protein folds that have evolved to function well at low temperatures. For example, type I AFP is a single free-standing alpha-helix,⁴⁷ and snow flea AFP has a polyproline II coil structure held together largely by a network of hydrogen bonds between the peptide backbones of the neighboring coils.^{45,48,49} Interestingly, the *LpIBP* structure lacks obvious N- or C-terminal capping structures that have been observed in most other beta-solenoid structures.^{37,50} While the larger side chains present on the N terminus of *LpIBP* may stabilize that end of the helix, the C terminus is left exposed. The lack of capping structures may explain why this IBP unfolds at temperatures above ~12 °C but readily refolds after heat treatment.^{31,51,52}

Steric mutagenesis is commonly used to deduce the location of an AFP's IBS.^{31,53–56} However, even non-steric mutants that do not disrupt the protein's fold can disrupt ice binding, possibly by disturbing the anchored-clathrate waters on the IBS. The replacement of regularly spaced Thr residues with Val *versus* Ser had very different effects on the activity of the alpha-helical type I AFP.^{57–59} Val was well tolerated, but Ser caused a large loss in TH activity. The subsequent identification of the IBS of type I AFP as a hydrophobic surface formed from the Thr_{*i*}, Ala_{*i*+4} and Ala_{*i*+8} in each TxxxAxxxAxx repeat⁵⁶ revealed the structural basis for the importance of the Thr methyl groups. In light of the anchored-clathrate hypothesis,¹⁵ the loss of the Thr methyl group (Ser replacement) would fragment the potential clathrate structure that may form along the length of the alpha-helix.

Substitution of single Thr residues on the IBS of *TmAFP* with Ser or Val both resulted in a large decrease in the TH activity in comparison with the

wild-type protein. The explanation for this decrease is twofold: the loss of the hydroxyl moiety as a result of the Thr-to-Val mutation means that the *TmAFP* mutant would be less able to secure its anchored-clathrate waters by hydrogen bonds; secondly, when a Thr is replaced with Ser, the loss of a beta-branched side chain is likely to release the locked conformations of the flanking Thr residues, further disrupting the bound clathrate waters. In addition, the gain (Val) or loss (Ser) of a methyl group could further perturb the anchored-clathrate structure.

A previous mutagenesis study of *TmAFP*'s IBS⁶⁰ replaced four of the central Thr residues with Val, which resulted in reduced TH activity similar to the level seen here with *LpIBP*. Mutating eight of the Thr residues to Val completely abolished TH, supporting our contention that the hydrogen-bonding capacity of the hydroxyl group is critical for ice binding. We hypothesize that the lower TH associated with *LpIBP* (Fig. 3c) is due to the decreased likelihood of the protein organizing a quorum of water molecules for ice binding due to the heterogeneity of the IBS residues. In support of this hypothesis, *LpIBP* is known to partition into growing ice poorly compared to wild-type AFPs.⁵² This behavior is consistent with AFPs bearing mutations that disrupt their IBSs and reduce TH activity. Indeed, *LpIBP* binds to ice using an imperfect hyperactive AFP IBS.

A defining characteristic of a hyperactive AFP is its affinity for the basal plane, which blocks ice crystal growth along the *c*-axis, thus protecting the crystal from growth down to lower freezing temperatures. Organisms that produce hyperactive AFPs (such as insects) are capable of surviving lower temperatures than those (like fish) with moderately active AFPs that do not adsorb to the basal plane. Basal-plane affinity was postulated to result from the spacing of the side chains on the IBS of beta-helical AFPs, which provides an almost exact match to the spacing of oxygen atoms on this plane of ice.^{33,34} More recently, it was proposed that this spacing is required to organize and anchor basal-plane ice-like waters on the IBS, which are then responsible for binding to ice.¹⁵ AFPs that are not hyperactive lack this particular spacing and do not have the capacity to bind the basal plane.

LpIBP appears to be an anomaly in that it has the ability to adhere to the basal plane of ice but possesses low TH activity. However, as documented here and elsewhere, mutation of an IBS can greatly lower or even eliminate TH.^{56,61} Thus, the heterogeneity of the IBS of *LpIBP* is predicted to lower the probability that the protein will acquire the minimum number of anchored waters to allow it to bind to ice. Consistent with this idea, the anchored water molecules on the *LpIBP* IBS form a looser network than those constrained by the more regular IBS of *MpAFP*.¹⁵

LpIBP presumably evolved to protect grass from damage caused by recrystallization of ice rather than to prevent freezing by depressing the freezing temperature. AFPs from freeze-avoiding organisms adsorb to ice to prevent its growth, allowing the surrounding liquid water to supercool. When the threshold temperature for freezing is breached, the ice crystals burst explosively, inflicting extensive tissue damage. Thus, it would be an impractical approach for plants that are routinely exposed to extreme sub-freezing conditions to attempt to prevent freezing using AFPs. Instead, some freeze-tolerant plants employ IBPs to minimize the damage associated with freezing.

A search of the expressed sequence tag and nucleotide databases for isoforms and homologues of *LpIBP* shows that *L. perenne* has at least three other *LpIBP* sequences. The sequences of several other grass IBP orthologues have been deposited, and in each species, the IBP has multiple isoforms.^{32,62–64} Alignments show that their IRI domains are composed of tandem repeats with the same consensus sequence (XXNXVXG) and include the same one-amino-acid insertion in their first three coils. The ice-binding residues are well conserved, but the other outward-projecting residues are highly variable. The structural residues within the beta-roll show high levels of conservation. In fact, the locations of the inward-pointing His residues are fully conserved in these isoforms, suggesting that they play an important structural role. Interestingly, like the insect AFPs, the largest variation between these orthologues and isoforms is the number of tandem repeats, which varies from 11 to 17. This strongly implies that each isoform has the same overall fold and these other sequences could be modeled based on *LpIBP*.

Based on the structure of *LpIBP*, we hypothesize that IBPs involved in IRI have lower TH activities than AFPs because their IBSs are less well ordered. As a result, they have fewer ice-like waters and a reduced ice-binding capacity. One way to test this hypothesis will be to solve additional IBP structures from organisms that tolerate freezing and compare them to AFPs. At the same time, it will be necessary to have an unrestricted view of their IBS in contact with water. Clearly, there is still much to be learned from pursuing the structural biology of IBPs.

Materials and Methods

Purification and crystallization of *LpIBP*

Recombinant *LpIBP* with a C-terminal 6×His-tag was purified in three steps as previously described.³¹ After removal of most contaminating *Escherichia coli* proteins by boiling, *LpIBP* was further purified by ice affinity purification,⁶⁵ which also selected for properly folded

LpIBP. Finally, Ni-Agarose affinity chromatography was performed, mainly to concentrate the His-tagged product. The pure protein was eluted and dialyzed against 50 mM Tris-HCl (pH 7.8), 100 mM NaCl and 1 mM ethylenediaminetetraacetic acid prior to crystal screening. Crystallization trials were done at 4 °C in 24-well 500-μL vapor diffusion plates (Hampton Research, Aliso Viejo, CA, USA) using 2 μL of protein at 10 mg/mL and 2 μL of mother liquor. Initial crystals were obtained under condition 18 of the JCSG+ Screen [40% ethanol, 5% polyethylene glycol 1000 and 100 mM phosphate-citrate (pH 4.2)] (Qiagen, Toronto, ON, Canada.) Crystals were optimized using a range of 40–50% ethanol, 100 mM phosphate-citrate (pH 4.1–4.3) and 0–5% polyethylene glycol 1000. Microseeding and macroseeding techniques were used to obtain diffraction-quality crystals, which typically took 3–4 weeks to grow. Optimized native crystals were approximately 0.2 mm × 0.1 mm × 0.05 mm and were soaked in 25% ethylene glycol, 40% ethanol and 50 mM phosphate-citrate (pH 4.2) before being flash-frozen in liquid nitrogen. For phasing, crystals were soaked in a variety of heavy metals at low concentration or in highly concentrated (0.5–1 M) halide salts.

Structure determination of *LpIBP*

Data were collected at 100 K from beamline X6A at Brookhaven National Laboratories (Upton, NY). Two crystals were used for structure determination: one native (collected at 1.13 Å) and one soaked for approximately 5 min in 1 M NaI, 25% ethylene glycol, 40% ethanol and 50 mM phosphate-citrate (pH 4.2) (collected at 1.55 Å). Data were indexed and integrated with XDS and scaled using XSCALE.⁶⁶ The two data sets were merged with CAD and scaled together with SCALEIT.⁶⁷ SHARP/ autoSHARP⁶⁸ was used to locate iodide sites and obtain phases using single isomorphous replacement with anomalous scattering. Sixteen iodide atoms were located, resulting in a phasing power of 1.32/0.96/0.77 (acentric/centric/anomalous), and solvent flattening determined that the crystals had a solvent content of 70%. Iterative model building was done with ARP/wARP,³⁶ and the resulting model was submitted to a cycle of simulated annealing at 3000 K followed by energy minimization and *B*-factor refinement cycle using Phenix-refine.⁶⁹ Afterwards, the model was refined by simple energy minimization followed by isotropic *B*-factor refinement (restrained and individual). Manual rebuilding, including adding alternate conformation of amino acids, was performed using Coot v0.6.2.⁷⁰ The final model was submitted to PROCHECK to ascertain its quality.⁷¹

TH measurements

TH measurements were made using a Clifton nanolitre osmometer (Clifton Technical Physics, Hartford, NY, USA) or a modified apparatus where the temperature of the cooled block was regulated by a Newport Temperature Controller (Model 3040), and the experiments were recorded to a computer using a video frame grabber (IMAQ PCI-1407; National Instruments Inc., Austin, TX). This system was controlled by the Labview software as described previously.⁷² A sample droplet of ~100 μm

diameter was flash-frozen and warmed until a single ice crystal remained. Once a crystal of desired size ($\sim 20\ \mu\text{m}$) was formed, the melting temperature was recorded, and the temperature was lowered at a rate of $0.01\ ^\circ\text{C}$ every 10 s until the ice crystal suddenly grew. This temperature was determined as the freezing point of the crystal, and the TH was the difference between this freezing point and the melting point.

FIPA analysis

FIPA analysis is a modification of ice binding plane analysis by sublimation (ice etching²³) and was performed as previously described.²⁵ A fluorescent-tagged IBP was engineered by ligating cDNA encoding GFP into the NdeI site upstream of the *LpIBP* coding sequence, leaving the C-terminal $6\times\text{His}$ -tag intact. The construct was sequenced before being transformed into *E. coli* strain BL21(DE3). The GFP-*LpIBP* fusion protein gene was expressed under the same conditions as the *LpIBP* gene. After cells were harvested by centrifugation and lysed by sonication, the lysate was centrifuged at $21,000g$. GFP-*LpIBP* was partially purified from the crude lysate supernatant by Ni-Agarose affinity chromatography (Ni-NTA; Qiagen). The tagged IBP was eluted from the column with 50 mM Tris-HCl (pH 7.8), 250 mM imidazole and 100 mM NaCl (5 mL) and dialyzed against 20 mM Tris-HCl and 20 mM NaCl before being used in FIPA analysis at a concentration of approximately 0.2 mg/mL. Photographs of hemispheres under ultraviolet illumination were taken with a Canon EOS 50D camera through a Canon EF 17- to 85-mm lens.

Mutagenesis and expression of TmAFP

TmAFP mutations were made using the Kunkel method.⁷³ Mutant proteins were produced and purified as previously described.⁵³ After the two-step purification, the *TmAFP* mutants were dialyzed against 100 mM NH_4HCO_3 for TH measurements at a range of AFP concentrations.

Structure deposition

The atomic coordinates and structure factors were submitted to the Research Collaboratory for Structural Bioinformatics Protein Data Bank (ID: 3ULT).

Acknowledgements

This research was funded by a grant to P.L.D. from the Canadian Institutes of Health Research. The authors thank Debborah Fass for the gift of GFP-*TmAFP*, Christopher Garnham for help growing ice crystal hemispheres, Jean Jakoncic and Vivian Stojanoff from beamline X6A at Brookhaven National Laboratory for beamline support, Margaret Daley and Brian Sykes for validating the folding of the *TmAFP* point mutations, Sherry Gauthier for

technical support, Zongchao Jia and John Allingham for access to their home-source beams and Qilu Ye for aiding with initial crystal screening. P.L.D. holds a Canada Research Chair in Protein Engineering, A.J.M. was supported by a Natural Sciences and Engineering Research Council of Canada Postgraduate Scholarship (PGS-D2), F.F. was supported by a postdoctoral fellowship from Fond de la Recherche en Santé du Québec, V.K.W. was supported by a Queen's Research Chair and M.B. was supported by the Lady Davis Fellowship Trust and by the Israel Science Foundation.

References

1. Jia, Z. & Davies, P. L. (2002). Antifreeze proteins: an unusual receptor–ligand interaction. *Trends Biochem. Sci.* **27**, 101–106.
2. Fletcher, G. L., Hew, C. L. & Davies, P. L. (2001). Antifreeze proteins of teleost fishes. *Annu. Rev. Physiol.* **63**, 359–390.
3. Urrutia, M. E., Duman, J. G. & Knight, C. A. (1992). Plant thermal hysteresis proteins. *Biochim. Biophys. Acta*, **1121**, 199–206.
4. Griffith, M. & Yaish, M. W. F. (2004). Antifreeze proteins in overwintering plants: a tale of two activities. *Trends Plant Sci.* **9**, 399–405.
5. DeVries, A. L. (1971). Glycoproteins as biological antifreeze agents in antarctic fishes. *Science*, **172**, 1152–1155.
6. Knight, C. A., DeVries, A. L. & Oolman, L. D. (1984). Fish antifreeze protein and the freezing and recrystallization of ice. *Nature*, **308**, 295–296.
7. Griffith, M., Lumb, C., Wiseman, S. B., Wisniewski, M., Johnson, R. W. & Marangoni, A. G. (2005). Antifreeze proteins modify the freezing process in plants. *Plant Physiol.* **138**, 330–340.
8. Sidebottom, C., Buckley, S., Pudney, P., Twigg, S., Jarman, C., Holt, C. *et al.* (2000). Heat-stable antifreeze protein from grass. *Nature*, **406**, 256.
9. Worrall, D., Elias, L., Ashford, D., Smallwood, M., Sidebottom, C., Lillford, P. *et al.* (1998). A carrot leucine-rich-repeat protein that inhibits ice recrystallization. *Science*, **282**, 115–117.
10. Yu, S. O., Brown, A., Middleton, A. J., Tomczak, M. M., Walker, V. K. & Davies, P. L. (2010). Ice restructuring inhibition activities in antifreeze proteins with distinct differences in thermal hysteresis. *Cryobiology*, **61**, 327–334.
11. Janech, M., Krell, A., Mock, T., Kang, J. & Raymond, J. (2006). Ice-binding proteins from sea ice diatoms (*Bacillariophyceae*). *J. Phycol.* **42**, 410–416.
12. Raymond, J. A. & DeVries, A. L. (1977). Adsorption inhibition as a mechanism of freezing resistance in polar fishes. *Proc. Natl Acad. Sci. USA*, **74**, 2589–2593.
13. Knight, C. A. (2000). Structural biology. Adding to the antifreeze agenda. *Nature*, **406**, 249–251.
14. Nutt, D. R. & Smith, J. C. (2008). Dual function of the hydration layer around an antifreeze protein revealed by atomistic molecular dynamics simulations. *J. Am. Chem. Soc.* **130**, 13066–13073.

15. Garnham, C. P., Campbell, R. L. & Davies, P. L. (2011). Anchored clathrate waters bind antifreeze proteins to ice. *Proc. Natl Acad. Sci. USA*, **108**, 7363–7367.
16. Yang, C. & Sharp, K. A. (2005). Hydrophobic tendency of polar group hydration as a major force in type I antifreeze protein recognition. *Proteins*, **59**, 266–274.
17. Schneppenheim, R. & Theede, H. (1980). Isolation and characterization of freezing-point depressing peptides from larvae of *Tenebrio molitor*. *Comp. Biochem. Physiol. B Comp. Biochem.* **67**, 561–568.
18. Hew, C. L., Kao, M. H., So, Y. P. & Lim, K. P. (1983). Presence of cystine-containing antifreeze proteins in the spruce budworm, *Choristoneura fumirana*. *Can. J. Zool.* **61**, 2324–2328.
19. Duman, J. G. (1977). Variations in macromolecular antifreeze levels in larvae of the darkling beetle, *Meracantha contracta*. *J. Exp. Zool.* **201**, 85–92.
20. Graham, L. A., Liou, Y. C., Walker, V. K. & Davies, P. L. (1997). Hyperactive antifreeze protein from beetles. *Nature*, **388**, 727–728.
21. Tyshenko, M. G., Doucet, D., Davies, P. L. & Walker, V. K. (1997). The antifreeze potential of the spruce budworm thermal hysteresis protein. *Nat. Biotechnol.* **15**, 887–890.
22. Scotter, A. J., Marshall, C. B., Graham, L. A., Gilbert, J. A., Garnham, C. P. & Davies, P. L. (2006). The basis for hyperactivity of antifreeze proteins. *Cryobiology*, **53**, 229–239.
23. Knight, C. A., Cheng, C. C. & DeVries, A. L. (1991). Adsorption of alpha-helical antifreeze peptides on specific ice crystal surface planes. *Biophys. J.* **59**, 409–418.
24. Antson, A. A., Smith, D. J., Roper, D. I., Lewis, S., Caves, L. S., Verma, C. S. *et al.* (2001). Understanding the mechanism of ice binding by type III antifreeze proteins. *J. Mol. Biol.* **305**, 875–889.
25. Garnham, C. P., Natarajan, A., Middleton, A. J., Kuiper, M. J., Braslavsky, I. & Davies, P. L. (2010). Compound ice-binding site of an antifreeze protein revealed by mutagenesis and fluorescent tagging. *Biochemistry*, **49**, 9063–9071.
26. Knight, C. A. & DeVries, A. L. (1988). The prevention of ice crystal growth from water by "Antifreeze Proteins". In *Atmospheric Aerosol and Nucleation* (Wagner, P. E. & Valli, G., eds), pp. 717–720, Springer, Berlin, Germany.
27. Pertaya, N., Marshall, C. B., Celik, Y., Davies, P. L. & Braslavsky, I. (2008). Direct visualization of spruce budworm antifreeze protein interacting with ice crystals: basal plane affinity confers hyperactivity. *Biophys. J.* **95**, 333–341.
28. Sandve, S. R., Kosmala, A., Rudi, H., Fjellheim, S., Rapacz, M., Yamada, T. & Rognli, O. A. (2011). Molecular mechanisms underlying frost tolerance in perennial grasses adapted to cold climates. *Plant Sci.* **180**, 69–77.
29. Gudleifsson, B., Andrews, C. & Bjornsson, H. (1986). Cold hardiness and ice tolerance of pasture grasses grown and tested in controlled environments. *Can. J. Plant Sci.* **66**, 601–608.
30. Andrews, C. (1996). How do plants survive ice. *Ann. Bot.* **78**, 529–536.
31. Middleton, A. J., Brown, A. M., Davies, P. L. & Walker, V. K. (2009). Identification of the ice-binding face of a plant antifreeze protein. *FEBS Lett.* **583**, 815–819.
32. Sandve, S. R., Rudi, H., Asp, T. & Rognli, O. A. (2008). Tracking the evolution of a cold stress associated gene family in cold tolerant grasses. *BMC Evol. Biol.* **8**, 245.
33. Liou, Y. C., Tocilj, A., Davies, P. L. & Jia, Z. (2000). Mimicry of ice structure by surface hydroxyls and water of a beta-helix antifreeze protein. *Nature*, **406**, 322–324.
34. Graether, S. P., Kuiper, M. J., Gagné, S. M., Walker, V. K., Jia, Z., Sykes, B. D. & Davies, P. L. (2000). Beta-helix structure and ice-binding properties of a hyperactive antifreeze protein from an insect. *Nature*, **406**, 325–328.
35. Kuiper, M. J., Davies, P. L. & Walker, V. K. (2001). A theoretical model of a plant antifreeze protein from *Lolium perenne*. *Biophys. J.* **81**, 3560–3565.
36. Langer, G., Cohen, S. X., Lamzin, V. S. & Perrakis, A. (2008). Automated macromolecular model building for X-ray crystallography using ARP/wARP version 7. *Nat. Protoc.* **3**, 1171–1179.
37. Kajava, A. V. & Steven, A. C. (2006). Beta-rolls, beta-helices, and other beta-solenoid proteins. *Adv. Protein Chem.* **73**, 55–96.
38. Holm, L. & Rosenström, P. (2010). Dali server: conservation mapping in 3D. *Nucleic Acids Res.* **38**, W545–W549.
39. Agnew, C., Borodina, E., Zaccari, N. R., Connors, R., Burton, N. M., Vicary, J. A. *et al.* (2011). Correlation of in situ mechanosensitive responses of the *Moraxella catarrhalis* adhesin UspA1 with fibronectin and receptor CEACAM1 binding. *Proc. Natl Acad. Sci. USA*, **108**, 15174–15178.
40. Xiang, Y., Leiman, P. G., Li, L., Grimes, S., Anderson, D. L. & Rossmann, M. G. (2009). Crystallographic insights into the autocatalytic assembly mechanism of a bacteriophage tail spike. *Mol. Cell*, **34**, 375–386.
41. Daley, M. E. & Sykes, B. D. (2004). Characterization of threonine side chain dynamics in an antifreeze protein using natural abundance ¹³C NMR spectroscopy. *J. Biomol. NMR*, **29**, 139–150.
42. Jia, Z., DeLuca, C. I., Chao, H. & Davies, P. L. (1996). Structural basis for the binding of a globular antifreeze protein to ice. *Nature*, **384**, 285–288.
43. Yang, D. S., Sax, M., Chakrabarty, A. & Hew, C. L. (1988). Crystal structure of an antifreeze polypeptide and its mechanistic implications. *Nature*, **333**, 232–237.
44. Tachibana, Y., Fletcher, G. L., Fujitani, N., Tsuda, S., Monde, K. & Nishimura, S. (2004). Antifreeze glycoproteins: elucidation of the structural motifs that are essential for antifreeze activity. *Angew. Chem., Int. Ed. Engl.* **43**, 856–862.
45. Pentelute, B. L., Gates, Z. P., Tereshko, V., Dashnau, J. L., Vanderkooi, J. M., Kossiakoff, A. A. & Kent, S. B. H. (2008). X-ray structure of snow flea antifreeze protein determined by racemic crystallization of synthetic protein enantiomers. *J. Am. Chem. Soc.* **130**, 9695–9701.
46. Gronwald, W., Loewen, M. C., Lix, B., Daugulis, A. J., Sönnichsen, F. D., Davies, P. L. & Sykes, B. D. (1998). The solution structure of type II antifreeze protein reveals a new member of the lectin family. *Biochemistry*, **37**, 4712–4721.

47. Sicheri, F. & Yang, D. S. (1995). Ice-binding structure and mechanism of an antifreeze protein from winter flounder. *Nature*, **375**, 427–431.
48. Lin, F., Graham, L. A., Campbell, R. L. & Davies, P. L. (2007). Structural modeling of snow flea antifreeze protein. *Biophys. J.* **92**, 1717–1723.
49. Pentelute, B. L., Gates, Z. P., Dashnau, J. L., Vanderkooi, J. M. & Kent, S. B. H. (2008). Mirror image forms of snow flea antifreeze protein prepared by total chemical synthesis have identical antifreeze activities. *J. Am. Chem. Soc.* **130**, 9702–9707.
50. Bryan, A. W. J., Starmer-Kreinbrink, J. L., Hosur, R., Clark, P. L. & Berger, B. (2011). Structure-based prediction reveals capping motifs that inhibit β -helix aggregation. *Proc. Natl Acad. Sci. USA*, **108**, 11099–11104.
51. Kumble, K. D., Demmer, J., Fish, S., Hall, C., Corrales, S., DeAth, A. *et al.* (2008). Characterization of a family of ice-active proteins from the Ryegrass, *Lolium perenne*. *Cryobiology*, **57**, 263–268.
52. Lauersen, K. J., Brown, A., Middleton, A., Davies, P. L. & Walker, V. K. (2011). Expression and characterization of an antifreeze protein from the perennial rye grass, *Lolium perenne*. *Cryobiology*, **62**, 194–201.
53. Marshall, C. B., Daley, M. E., Graham, L. A., Sykes, B. D. & Davies, P. L. (2002). Identification of the ice-binding face of antifreeze protein from *Tenebrio molitor*. *FEBS Lett.* **529**, 261–267.
54. Garnham, C. P., Gilbert, J. A., Hartman, C. P., Campbell, R. L., Laybourn-Parry, J. & Davies, P. L. (2008). A Ca^{2+} -dependent bacterial antifreeze protein domain has a novel beta-helical ice-binding fold. *Biochem. J.* **411**, 171–180.
55. DeLuca, C. I., Davies, P. L., Ye, Q. & Jia, Z. (1998). The effects of steric mutations on the structure of type III antifreeze protein and its interaction with ice. *J. Mol. Biol.* **275**, 515–525.
56. Baardsnes, J., Kondejewski, L. H., Hodges, R. S., Chao, H., Kay, C. & Davies, P. L. (1999). New ice-binding face for type I antifreeze protein. *FEBS Lett.* **463**, 87–91.
57. Chao, H., Houston, M. E. J., Hodges, R. S., Kay, C. M., Sykes, B. D., Loewen, M. C. *et al.* (1997). A diminished role for hydrogen bonds in antifreeze protein binding to ice. *Biochemistry*, **36**, 14652–14660.
58. Haymet, A. D., Ward, L. G., Harding, M. M. & Knight, C. A. (1998). Valine substituted winter flounder 'antifreeze': preservation of ice growth hysteresis. *FEBS Lett.* **430**, 301–306.
59. Zhang, W. & Laursen, R. A. (1998). Structure–function relationships in a type I antifreeze polypeptide. The role of threonine methyl and hydroxyl groups in antifreeze activity. *J. Biol. Chem.* **273**, 34806–34812.
60. Bar, M., Celik, Y., Fass, D. & Braslavsky, I. (2008). Interactions of β -helical antifreeze protein mutants with ice. *Cryst. Growth Des.* **8**, 2954–2963.
61. Baardsnes, J., Jelokhani-Niaraki, M., Kondejewski, L. H., Kuiper, M. J., Kay, C. M., Hodges, R. S. & Davies, P. L. (2001). Antifreeze protein from shorthorn sculpin: identification of the ice-binding surface. *Protein Sci.* **10**, 2566–2576.
62. Matsumoto, T., Tanaka, T., Sakai, H., Amano, N., Kanamori, H., Kurita, K. *et al.* (2011). Comprehensive sequence analysis of 24,783 barley full-length cDNAs derived from 12 clone libraries. *Plant Physiol.* **156**, 20–28.
63. John, U. P., Polotnianka, R. M., Sivakumaran, K. A., Chew, O., Mackin, L., Kuiper, M. J. *et al.* (2009). Ice recrystallization inhibition proteins (IRIPs) and freeze tolerance in the cryophilic Antarctic hair grass *Deschampsia antarctica* E. Desv. *Plant Cell Environ.* **32**, 336–348.
64. Tremblay, K., Ouellet, F., Fournier, J., Danyluk, J. & Sarhan, F. (2005). Molecular characterization and origin of novel bipartite cold-regulated ice recrystallization inhibition proteins from cereals. *Plant Cell Physiol.* **46**, 884–891.
65. Kuiper, M. J., Lankin, C., Gauthier, S. Y., Walker, V. K. & Davies, P. L. (2003). Purification of antifreeze proteins by adsorption to ice. *Biochem. Biophys. Res. Commun.* **300**, 645–648.
66. Kabsch, W. (2010). XDS. *Acta Crystallogr., Sect. D: Biol. Crystallogr.* **66**, 125–132.
67. Collaborative Computational Project. (1994). The CCP4 suite: programs for protein crystallography. *Acta Crystallogr., Sect. D: Biol. Crystallogr.* **50**, 760–763.
68. Vonrhein, C., Blanc, E., Roversi, P. & Bricogne, G. (2007). Automated structure solution with auto-SHARP. *Methods Mol. Biol.* **364**, 215–230.
69. Adams, P. D., Afonine, P. V., Bunkóczi, G., Chen, V. B., Davis, I. W., Echols, N. *et al.* (2010). PHENIX: a comprehensive Python-based system for macromolecular structure solution. *Acta Crystallogr., Sect. D: Biol. Crystallogr.* **66**, 213–221.
70. Emsley, P., Lohkamp, B., Scott, W. G. & Cowtan, K. (2010). Features and development of Coot. *Acta Crystallogr., Sect. D: Biol. Crystallogr.* **66**, 486–501.
71. Laskowski, R. A., MacArthur, M. W., Moss, D. S. & Thornton, J. M. (1993). PROCHECK: a program to check the stereochemical quality of protein structures. *J. Appl. Crystallogr.* **26**, 283–291.
72. Celik, Y., Graham, L. A., Mok, Y., Bar, M., Davies, P. L. & Braslavsky, I. (2010). Superheating of ice crystals in antifreeze protein solutions. *Proc. Natl Acad. Sci. USA*, **107**, 5423–5428.
73. Kunkel, T. A., Roberts, J. D. & Zakour, R. A. (1987). Rapid and efficient site-specific mutagenesis without phenotypic selection. *Methods Enzymol.* **154**, 367–382.